JPhys Energy

The effect of configurational entropy on acoustic emission of P2-type layered oxide cathodes for sodium-ion batteries

To cite this article: Sören L Dreyer *et al* 2023 *J. Phys. Energy* **5** 035002

IOP Publishing J. Phys. Energy 5 (2023) 035002 https://doi.org/10.1088/2515-7655/acd41a

Journal of Physics: Energy

OPEN ACCESS

RECEIVED
27 January 2023

REVISED
3 May 2023

ACCEPTED FOR PUBLICATION
10 May 2023

PUBLISHED
19 May 2023

PAPER

The effect of configurational entropy on acoustic emission of P2-type layered oxide cathodes for sodium-ion batteries

Sören L Dreyer[1], Ruizhuo Zhang[1], Junbo Wang[1], Aleksandr Kondrakov[2], Qingsong Wang[1,3,*], Torsten Brezesinski[1,*] and Jürgen Janek[1,4]

[1] Institute of Nanotechnology, Karlsruhe Institute of Technology (KIT), Hermann-von-Helmholtz-Platz 1, 76344 Eggenstein-Leopoldshafen, Germany
[2] BASF SE, Carl-Bosch-Str. 38, 67056 Ludwigshafen, Germany
[3] Bavarian Center for Battery Technology (BayBatt), Department of Chemistry, University of Bayreuth, Universitätsstr. 30, 95447 Bayreuth, Germany
[4] Institute of Physical Chemistry & Center for Materials Research (ZfM/LaMa), Justus-Liebig-University Giessen, Heinrich-Buff-Ring 17, 35392 Giessen, Germany
[*] Authors to whom any correspondence should be addressed.

E-mail: qingsong.wang@uni-bayreuth.de and torsten.brezesinski@kit.edu

Keywords: acoustic emission, P2-type layered cathode, high-entropy oxide, sodium-ion battery, chemo-mechanical degradation

Supplementary material for this article is available online

Abstract

Sodium-ion batteries (SIBs) see intensive research and commercialization efforts, aiming to establish them as an alternative to lithium-ion batteries. Among the reported cathode material families for SIBs, Na-deficient P2-type layered oxides are promising candidates, benefiting from fast sodium diffusion and therefore high charge/discharge rates. However, upon sodium extraction at high potentials, a transition from the P2 to O2 phase occurs, with the corresponding change in cell volume resulting in particle fracture and capacity degradation. A possible solution to this is to increase configurational entropy by introducing more elements into the transition-metal layer (so-called high-entropy concept), leading to some kind of structural stabilization. In this work, the acoustic emission (AE) of a series of P2-type layered oxide cathodes with increasing configurational entropy [$Na_{0.67}(Mn_{0.55}Ni_{0.21}Co_{0.24})O_2$, $Na_{0.67}(Mn_{0.45}Ni_{0.18}Co_{0.24}Ti_{0.1}Mg_{0.03})O_2$ and $Na_{0.67}(Mn_{0.45}Ni_{0.18}Co_{0.18}Ti_{0.1}Mg_{0.03}Al_{0.04}Fe_{0.02})O_2$] is recorded during SIB operation and correlated to the materials properties, namely change in *c* lattice parameter and cracking behavior. A structure-property relationship between entropy, manifested in the extent of phase transition, and detected AE is derived, supported by the classification of signals by peak frequency. This classification in combination with microscopy imaging allows to distinguish between inter- and intragranular fracture. Relatively more intergranular and less intragranular crack formation is observed with increasing configurational entropy.

1. Introduction

Low cost and high abundancy of sodium, relative to lithium, are key driving forces in the research and development of sodium-ion batteries (SIBs) as a complementary and sustainable energy-storage alternative to lithium-ion batteries (LIBs) [1]. This development is aided and accelerated by the similarity of the two technologies, allowing for fast transfer of concepts and solutions [2]. An example are the cathode active material (CAM) families where for both SIBs and LIBs polyanionic structures [e.g. $LiFePO_4$ and $NaFePO_4$ or $Na_3V_2(PO_4)_2F_3$] and layered oxides are most common, depending on the required energy density and cost sensitivity [1–3].

Layered oxides for SIBs are mostly of either O3 or P2 type, which differ in the coordination and amount of Na^+ per formula unit, with P2 generally being Na-deficient and Mn-rich, but with a more open framework structure allowing fast ion diffusion through direct prismatic paths [3–5]. However, upon sodium extraction, P2-type structures ($P6_3/mmc$ space group) undergo a transition towards the O2 phase ($P6_3mc$ space group),

similar to the H2–H3 phase transition in layered Ni-rich oxide cathodes for LIBs, such as $LiNiO_2$ [6–9]. The continuous phase transition and associated anisotropic cell volume changes lead to the formation of cracks in CAM particles and therefore material and performance degradation [8, 9]. For this reason, effectively mitigating or suppressing the phase transition and instead obtaining a solid-solution-like single-phase de/sodiation behavior is a widely researched pathway towards more stable P2-type CAMs. Stability improvements can, for example, be achieved by optimized synthesis conditions [10] or particle coatings. [11, 12] The most common strategy to suppress phase transitions and associated volume changes is doping, either by single elements, such as Mg [13], Fe [14] and Ru [15], or by multielement substitution [16, 17].

The introduction of a large number of elements into a single-phase structure is often referred to as the high-entropy (HE) concept, yielding high configurational entropy, in an attempt to achieve entropy-mediated (structural) stabilization and improved material properties by the so-called cocktail effect [18–20]. Initially proven with metal alloys, the HE approach has been applied recently to organic-inorganic hybrid and (oxide) ceramic battery cathodes and anodes [21–24]. For SIBs, this includes Prussian blue analogues [25, 26] and O3- and P2-type oxides, such as $Na(Ni_{0.12}Cu_{0.12}Mg_{0.12}Fe_{0.15}Co_{0.15}Mn_{0.1}Ti_{0.1}Sn_{0.1}Sb_{0.04})O_2$ and $Na_{0.62}(Mn_{0.67}Ni_{0.23}Cu_{0.05}Mg_{0.07}Ti_{0.01})O_2$ [17, 27–29]. Recently, we have reported a series of P2-type layered oxide CAMs with gradually increasing entropy for SIB applications, namely $Na_{0.67}(Mn_{0.55}Ni_{0.21}Co_{0.24})O_2$, $Na_{0.67}(Mn_{0.45}Ni_{0.18}Co_{0.24}Ti_{0.1}Mg_{0.03})O_2$ and $Na_{0.67}(Mn_{0.45}Ni_{0.18}Co_{0.18}Ti_{0.1}Mg_{0.03}Al_{0.04}Fe_{0.02})O_2$, which will be referred to as 3-$NTMO_2$, 5-$NTMO_2$ and 7-$NTMO_2$, respectively, in the following. They possess configurational entropies of 0.99R, 1.34R and 1.52R, where R is the universal gas constant [30]. For these materials, we observed increased reversibility with increasing entropy, as the degradative P2–O2 phase transition was reduced, with the 7-$NTMO_2$ material displaying solid-solution behavior upon sodium extraction. The mitigation of both manganese dissolution and gas evolution was also demonstrated.

The investigation of processes leading to performance degradation is either performed *ex situ*/*post-mortem*, i.e. on disassembled cell parts after the end of operation, or *in situ*/*operando*, i.e. in real-time during cell cycling. A variety of *in situ* characterization techniques has been reported for batteries based mostly on interaction combinations of photons and electrons with the respective materials [31]. Exceptions to this broad generalization are, for example, neutron diffraction and imaging [32], techniques used for gas analysis, such as differential electrochemical mass spectrometry (DEMS) [33], and acoustic techniques. The latter can be separated into active monitoring, wherein an (ultrasonic) acoustic signal is generated externally and its propagation in the battery cell is studied [34–36], and passive monitoring, where acoustic signals emitted from the object under investigation are recorded, the so-called acoustic emission (AE) technique [37]. Acoustic waves can appear in various types and forms, but ultimately all originating from plastic deformation and cracking (i.e. local structural rearrangement), leading to a reduction in strain energy [37–39].

AE as a real-time, non-destructive and non-invasive technique has seen wide application in structural health monitoring, such as detecting fatigue and crack formation in construction materials [38]. For battery cells, AE has been used to monitor the state of health and predict the remaining cycle life [40–42]. However, AE monitoring in batteries is not limited to the cell as a whole, but can be applied to characterize individual electrodes. Various electrode materials have been studied by AE, including CAMs [e.g. $LiCoO_2$ [43], $LiMnO_2$ [44], $LiNiO_2$ [39] and HE $Li_x(Co_{0.2}Cu_{0.2}Mg_{0.2}Ni_{0.2}Zn_{0.2})OF_x$ [45]] and anode active materials [e.g. graphite [46], silicon [47–49], $NiSb_2$ [50] and HE $(Co_{0.2}Cu_{0.2}Mg_{0.2}Ni_{0.2}Zn_{0.2})O$ [51]]. For these materials, analysis of AE signals, with a single acoustic event usually referred to as a hit, allows gaining insights into solid electrolyte interphase (SEI) formation on the one hand and crack formation and propagation both on the particle and electrode level on the other hand. These processes can be distinguished by signal classification due to acoustic wave characteristics, such as peak frequency, rise time, duration or amplitude [39, 43–47, 51].

In the present work, we study and compare the aforementioned 3-$NTMO_2$, 5-$NTMO_2$ and 7-$NTMO_2$ SIB CAMs by AE, observing the effect of increasing configurational entropy as a change in phase-transition behavior (two-phase reaction versus solid solution), which results in different acoustic signatures of the associated crack formation. In so doing, inter- and intragranular particle fracture can be distinguished from one another.

2. Materials and methods

The materials were synthesized via solid-state reaction as described previously [30]. Electrodes were prepared by dispersing CAM (70 wt.%), carbon black (20 wt.%; Super C65, Imerys Graphite & Carbon) and polyvinylidene difluoride binder (10 wt.%; Solef 5130, Solvay) in *N*-methyl-2-pyrrolidone (Merck) and casting the resulting slurry on an Al current collector foil. For this study, electrodes with an active material loading of 8 mg cm^{-2} were produced. Disks of 13 mm diameter were punched out and dried overnight.

CR2032 coin cells (Hohsen) were then assembled inside an Ar-filled glovebox. Na metal and GF/D glass fiber filter paper (Whatman) were used as anode and separator, respectively. 95 μl of a 1.0 mol l^{-1} solution of $NaClO_4$ in ethylene carbonate, dimethyl carbonate and propylene carbonate (1:1:1 by volume) containing 5 vol.% fluoroethylene carbonate (FEC) was used as electrolyte.

For *operando* AE measurements, cells were cycled at 25 °C and at a rate of 0.1C, assuming 1C to be 200 mA g^{-1}, between 1.5 and 4.6 V vs. Na^+/Na using a BAT-SMALL potentiostat (Astrol Electronic AG). AE signals were recorded by a differential wideband sensor (125–1000 kHz; Mistras Group, Inc.) attached to the bottom of the coin cell using vacuum grease to improve contact. The setup further included an in-line preamplifier and a data acquisition system (USB AE Node; Mistras Group, Inc.). The preamp gain, analog filter and sampling rate were set to 40 dB, 20–1000 kHz and 5 MSPS, respectively. The sensor coupling was verified by the pencil-lead break test [52]. For each material, at least two samples were tested to ensure reproducibility. The AE setup and analysis procedure are described in more detail in the literature [39, 44–48, 51, 53]. Recordings were first processed by the AEwin software (Mistras Group, Inc.), filtering out background noise by eliminating all hits with less than two counts, peak frequencies lower than 100 kHz or amplitudes less than 27 dB, and then analyzed together with the respective electrochemical measurement data.

For *post-mortem* analysis, cells were cycled at 25 °C and 0.1C rate for up to 50 cycles using a Series 4000 battery test system (MACCOR), then crimped open and the cathode was washed with dimethyl carbonate to be recovered.

Scanning electron microscopy (SEM) was carried out on a LEO 1530 microscope (Zeiss) at 10 kV. For the preparation of cross-sectional images, an IB-19510CP cross-section polisher (JEOL) with Ar-gas source was used to polish the cathode in the pristine and cycled states. The respective SEM images were recorded under the same conditions as mentioned above.

Operando X-ray diffraction (XRD) measurements were carried out on a STOE Stadi P diffractometer (Ga K_β radiation, $\lambda = 1.20793$ Å). Further details can be found in the previous work [30]. Rietveld refinement and LeBail fitting were performed with the FullProf software package. Rietveld refinements of diffraction patterns collected from the pristine powders and the *operando* cells before electrochemical testing were first conducted to determine the zero shift. The zero shift was then kept constant for the LeBail fitting of the following patterns obtained during the charge/discharge process. Additionally, a larger hexagonal unit cell described by the space group $P6_3$ instead of $P6_3/mmc$ was considered for data refinement [54, 55].

3. Results and discussion

As previously reported, two potential ranges were explored in testing the cycling performance of the materials, one of them allowing for further reduction and possible disproportionation and dissolution of Mn [30]. For AE measurements, the wider range of 1.5–4.6 V vs. Na^+/Na was chosen, as it yields greater cell capacities and allows the Mn dissolution to be investigated. Figure 1(a) shows the specific charge/discharge capacities of 3-$NTMO_2$, 5-$NTMO_2$ and 7-$NTMO_2$ in coin half-cells cycled at 0.1C rate in the AE setup. The observed reduced charge capacity in the first cycle (q_{ch} = 142–143 mAh g^{-1}) is due to the intrinsic sodium deficiency of as-synthesized P2-type structures. The capacities are in line with those reported earlier when considering the different C-rates and also regarding the initial increase seen for 5-$NTMO_2$ and 7-$NTMO_2$ over the first few cycles [30]. The voltage profiles for the first five cycles are shown together with the cumulative number of AE hits and normalized hit rate for each material in figures 1(b)–(d).

The vast majority of hits are detected during charge, and with the exception of the first cycle, in the potential range from 4.2 to 4.6 V vs. Na^+/Na. In the initial cycle, hits are also detected below 4.2 V, starting from the beginning of charge. This is commonly attributed to the formation of the (cathode) SEI [39, 43, 45, 47, 56], as also observed for $LiCoO_2$ [43] and $LiNiO_2$ [39]. In anode active materials, the corresponding early SEI formation is also detectable via AE [46, 49, 51]. In agreement with previous results, the largest share of acoustic activity is observed in the potential range where particle cracking due to phase transitions and/or intense volume changes occurs, with the number of new hits per cycle slowly decreasing [39, 43–45, 57, 58]. Virtually no hits are detected at low potentials near the end of discharge, suggesting that the Mn reduction/disproportionation and CO_2 evolution due to FEC reduction, both of which are evident under these conditions [30], are not acoustically active. While the AE of gassing and subsequent bursting of gas bubbles is sometimes described in the literature [43, 46], it is further characterized by low peak frequencies and long rise times [56, 58–61] so that the attribution can be challenged if these conditions are not met by a given hit [39, 44, 47, 49]. In the setup used herein, gas evolution (detected via DEMS) was not [39, 51], or presumably only at extreme rates [45], observed by AE.

In general, the acoustic profiles appear simpler and clearer, due to high concentration of hits into a narrow voltage range, than those of CAMs for LIBs previously studied using the same setup [39, 45]. A likely

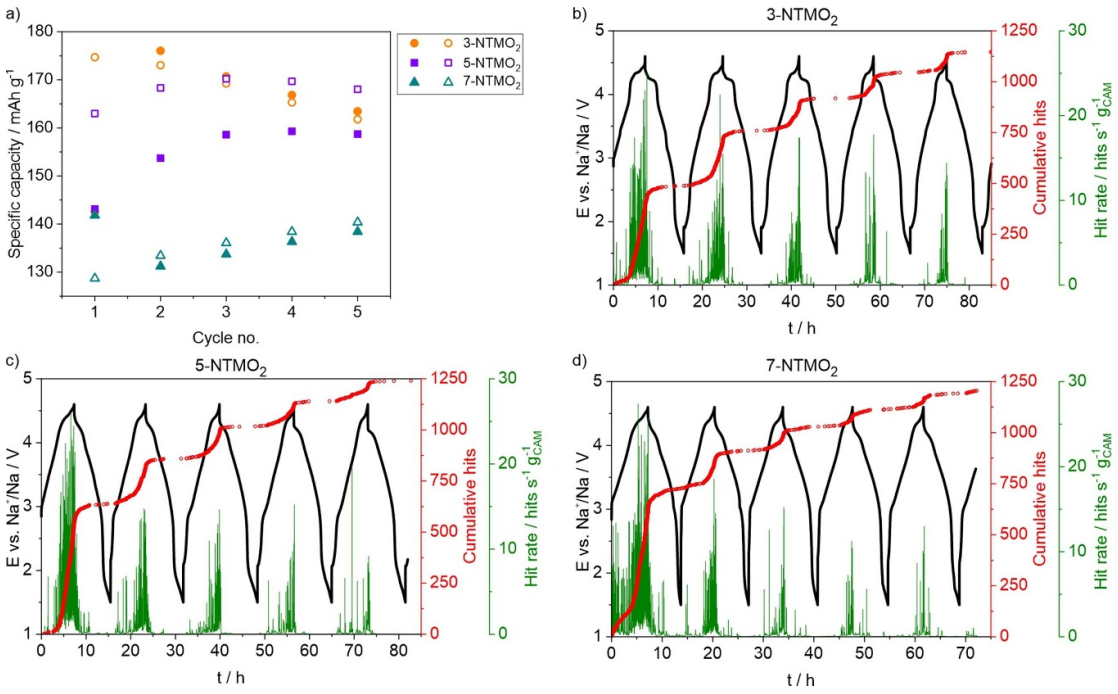

Figure 1. (a) Specific charge (solid symbols) and discharge capacities (hollow symbols) of 3-, 5- and 7-$NTMO_2$ and (b)–(d) corresponding acoustic profiles.

contribution to this is the morphology, with the materials studied herein consisting of micron-sized, monolithic (yet agglomerated) particles, while the LIB CAMs either consisted of primary particles agglomerated to micron-sized secondary particles [39] or nanoparticles [45]. Thus, a lower specific surface area and reduced contribution from surface side reactions can be expected. The particle size distribution of all three materials is shown in figure S1, with D_{50} between 9.4 μm (for 7-$NTMO_2$) and 12.4 μm (for 5-$NTMO_2$).

The apparent straightforwardness of the acoustic profiles not only allows, for the first time, characterizing different materials, but also comparing them. However, when comparing the different materials to one another, it should be considered that the similar number of hits detected after five cycles, as indicated in figures 1(b)–(d), is merely coincidental, as with the experimental setup used, the degree of acoustic transmission varies with the quality of contact between cell and sensor (screw pressure, amount of grease etc.), as well as with the individual coin cell (electrode alignment, crimping etc.). It is therefore hardly possible to directly compare absolute numbers. Instead, relative hits, i.e. normalized to the respective total number of hits, should be used. In figures 1(b)–(d), absolute numbers are shown for simplicity. Figure S2 represents the acoustic profiles of a second set of cells with normalized hits, thus also demonstrating the repeatability of the obtained results.

Because the AE is concentrated in the phase-transition region, figure S3 shows dq/dV plots for each material in this potential range during the first and second charge cycles. It is worth noting that the specific capacity stemming from desodiation above 4.0 V vs. Na^+/Na is similar between the materials, as shown in table S1, since differences in total capacity result mostly from a different degree of low-potential Mn^{3+} redox [30]. For the 3-$NTMO_2$ sample, a sharp main peak is observed around 4.35 V, corresponding to the voltage plateau in figure 1(b) and transition to the O2 phase, as previously found by *operando* XRD [30]. A shoulder at 4.2–4.3 V is believed to be related to lattice oxygen loss. It coincides with strong gas evolution in DEMS and is not seen during discharge, indicating an irreversible process [30]. The acoustic activity is concentrated within this phase-transition region, resulting in an S-shaped curve with little hits above 4.45 V in both cycles. The maximum gas evolution occurs around 4.3 V in the initial cycle, but above 4.45 V in the second one. Yet, the acoustic profile shapes are similar and do not show considerable activity above 4.45 V, and it can be concluded that high-potential gas evolution, including that associated with irreversible oxygen redox [33], is also not detected via AE in the given setup. For 5-$NTMO_2$ and especially the 7-$NTMO_2$ sample, on the other hand, a broader dq/dV peak without distinct lower shoulder is observed (figure S3), indicating a more solid-solution-like desodiation process, as also found via *operando* XRD [30]. At the same time, the hit curve changes from S-shape to a rather linear shape, including continuous hit detection at potentials above 4.45 V.

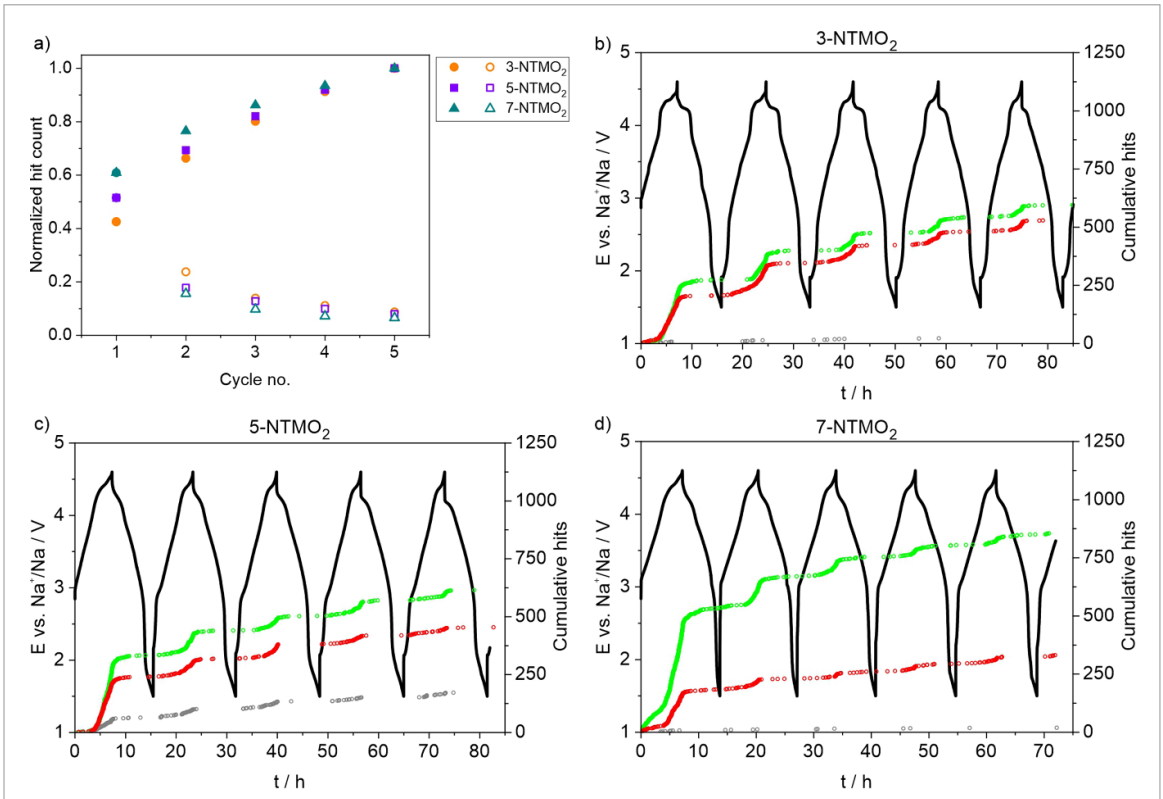

Figure 2. (a) Normalized hit count (solid symbols) and hits per cycle (hollow symbols) for 3-, 5- and 7-$NTMO_2$ and (b)–(d) corresponding acoustic profiles after classification by peak frequency into AE1 (gray), AE2 (red) and AE3 (green).

When considering the cumulative hits in the initial cycle according to figures 1(b)–(d) and S3 under the restriction of similar absolute numbers as discussed previously, it can be concluded that with increasing configurational entropy a larger amount of hits is detected, with less hits in the following cycles (i.e. flatter steps in the acoustic profiles in the later cycles).

Figure 2(a) shows the cumulative hits and hits per cycle for each material normalized to the total number after five cycles, confirming the trend towards concentration of AE into the first charge from 3-$NTMO_2$ to 7-$NTMO_2$. The hits are characterized further by additional parameters that can be used to classify AE events. While principal component analysis allows for the consideration of each parameter's contribution [47, 62], it is often found that the peak frequency is the most distinctive and allows to correlate AE hits with likely processes of their origin [43, 44, 47, 56–61]. For each material, hits are thus classified into three groups (AE1, AE2 and AE3) according to the peak frequency (<200, 200–300 and >300 kHz). In recent years, it has been found that low peak frequencies are often associated with gas bubble evolution or interfacial reactions, such as SEI formation, while higher frequencies can be attributed to mechanical stress-release processes, such as crack formation [43, 56, 58–62]. In some instances, AE classification by peak frequency is used to distinguish mechanical processes on different length scales, i.e. from microcrack formation over intragranular crack propagation/growth to intergranular (electrode) fracture, including deagglomeration of secondary particles [45, 47, 51].

Figures 2(b)–(d) show the acoustic profiles after classification by peak frequency and figure S4 presents histograms of frequency distribution. For the second set of cells (as shown in figure S2), figure S5 displays the normalized hit count. While 3-$NTMO_2$ and 7-$NTMO_2$ only show a negligible amount of AE1 activity, a few such hits were detected for 5-$NTMO_2$. Although low peak frequencies, as for AE1, are sometimes associated with gas evolution [43, 56, 58–61], all materials tested herein showed gassing of similar degree in the initial cycle [30], and other gas evolving processes have been ruled out above. Other processes in the AE1 range include electrode surface restructuring and SEI formation. A possible explanation therefore is an increased amount of surface impurities resulting in higher reactivity and AE from decomposition reactions. This assumption is supported by the slightly higher CO_2 evolution for 5-$NTMO_2$, which may indicate a larger concentration of residual carbonates on the surface [30, 33]. However, the main difference between the materials is found in the distribution of hits between AE2 and AE3. While 3-$NTMO_2$ shows only slightly more AE3 than AE2 hits, there is an increase in the share and total number of AE3 hits with increasing configurational entropy. Conversely, the share and total number of AE2 hits decreases. Considering prior AE

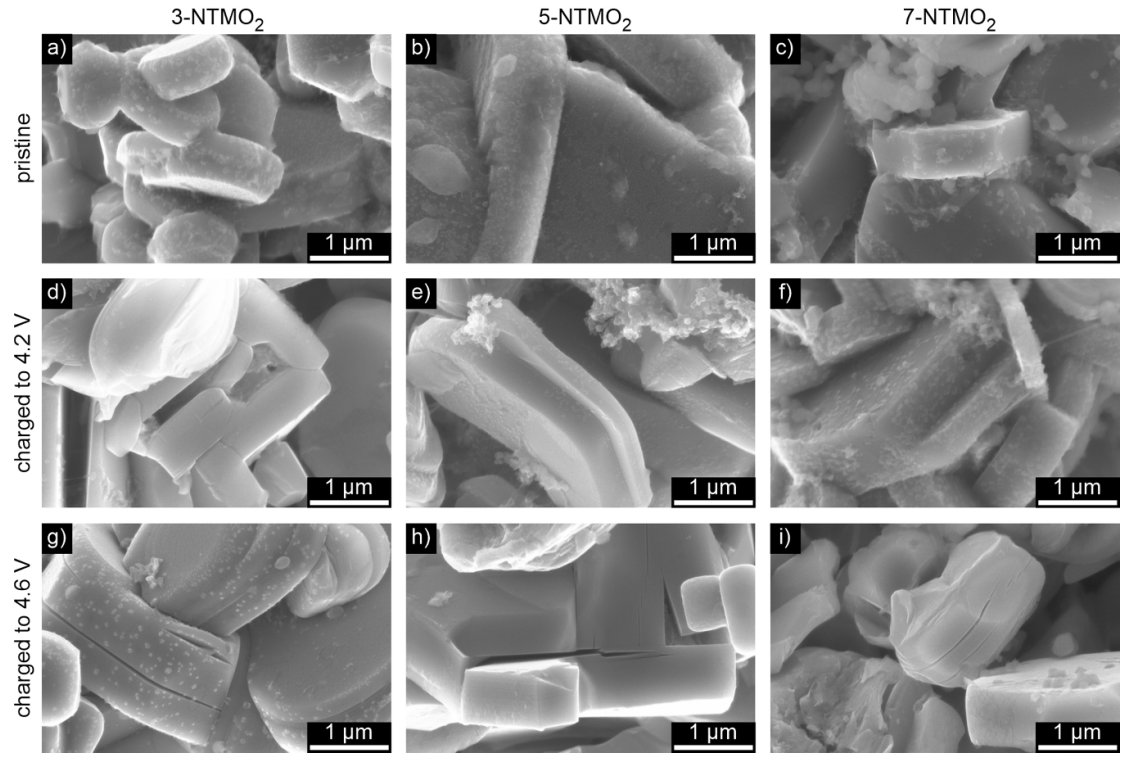

Figure 3. Top-view SEM images of pristine and charged (initial cycle) 3-, 5- and 7-$NTMO_2$ cathodes.

classification findings that show a relation between peak frequency and crack type or length scale/dimension [45, 47, 51], a likely hypothesis is that AE2 and AE3 represent the formation of one crack type each. As both a lower share of AE2 hits and lower degree of phase transition (or corresponding volume change) are observed with increasing configurational entropy in the materials, AE2 hits appear to be associated with the formation of intragranular cracks. Under this hypothesis, AE3 hits are then attributed to the formation of intergranular cracks, as was proposed in a previous study [45].

To correlate the observed differences in AE characterization and classification with material properties and especially to confirm the hypothesis regarding intragranular crack evolution and deagglomeration (intergranular cracking), *post-mortem* investigation of cycled electrodes was carried out. Figures 3(a)–(i) show top-view SEM images of the different CAMs in the pristine state and after charging to 4.2 V vs. Na^+/Na ($q_{ch} \approx 80$ mAh g^{-1}), i.e. prior to the onset of any phase transitions and appearance of most acoustic activity, and to 4.6 V, the cutoff potential with maximum change in lattice parameters according to *operando* XRD. In the pristine cathodes, the CAM particles are crack free and agglomerated or even sintered together. After charging to 4.2 V, small contact lines between the particles become visible and few initial intragranular cracks appear. At 4.6 V, more of these parallel-oriented crack lines can be observed and agglomerated particles have partially deagglomerated, as is evident from the presence of intergranular cracks. A voltage-plateau-dependent fracture behavior, with cracks oriented in parallel to the (002) plane, was previously reported for $Na_{2/3}Ni_{1/3}Mn_{2/3}O_2$, wherein Mg doping reduced the cracking tendency [9, 13]. Comparable behavior, including fracture along the (003) plane and the distinction of intra- and intergranular cracking, is also found in layered oxide LIB CAMs [63–65].

Cracks are usually formed because of anisotropic changes in unit cell volume. In this case, the particles first slightly expand during desodiation before the lattice collapses and shrinks at high states of charge [30, 66]. To quantitatively compare the root cause of particle fracture, *operando* XRD patterns were refined. The changes in lattice parameter *c* in the initial cycle are displayed in figure 4. In general, upon charging below 4.2 V, the extraction of Na^+ ions leads to increased repulsion of the oxygen layers (reduced shielding by the Na^+ ions), thus an increase in *c* is observed. During further desodiation, phase transition from P2 to O2 is prompted by the TMO_2 (or MO_2, to be more precise) slabs gliding in the *a*-*b* plane, because the empty prismatic sites are thermodynamically unstable [67]. Through metal substitution (HE approach), the P2-O2 transition is suppressed effectively and transferred to P2 to OP4 evolution in the case of 7-$NTMO_2$ (figure 4). The intergrown OP4 phase describes the alternate piling up (with possible stacking fault) of octahedral and trigonal prismatic layers (Na^+ ions are accommodated at the octahedral and prismatic sites) along the *c* axis. Overall, the P2–OP4 phase transition is more reversible [67]. The 5-$NTMO_2$ sample with medium

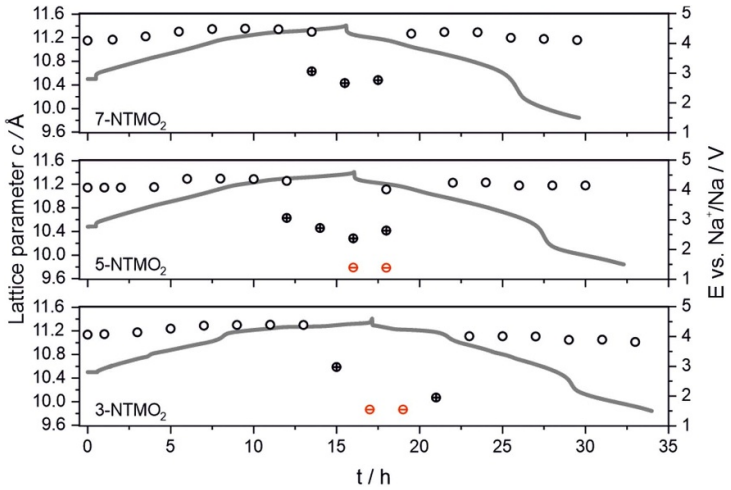

Figure 4. Changes in *c* lattice parameters during the initial cycle and corresponding phases (OP4 = black plus sign, O2 = red minus sign) at high potentials. The corresponding voltage profiles are shown in light gray. The error bars are included in the symbols.

configurational entropy shows existence of both the O2 and OP4 phases at high states of charge (figure 4). In the case of 3-$NTMO_2$, a complete transition (collapse in *c* axis) to O2 is observed at high potentials (figure 4). Hence, more severe lattice parameter/unit cell volume changes in 3-$NTMO_2$ lead to more particle fracture, supporting the assignment of AE2 hits to intergranular cracking.

Figure S6 shows additional top-view SEM images of particles at the end of discharge after both one and five cycles, demonstrating that cracks do not disappear after resodiation and return to the initial unit cell volume, while the occurrence of intragranular cracks and associated phenomena, such as delamination, exfoliation and electrochemical creep [17, 68–70], increases with the number of cycles. Top-view imaging relies on particles on the electrode surface after assembly and the study of deagglomeration is complicated by loss of such particles from the surface. For this reason, ion milling was carried out and the resulting cross sections were studied via SEM. For both 3- and 7-$NTMO_2$, figures 5(a)–(h) and S7 show images collected from the cathodes before and after cycling (1, 5 and 50 cycles). In cycled electrodes, not only the formation of intragranular crack planes, visible as parallel lines, can be observed, but also the expansive delamination and exfoliation of cracked (single-crystalline) particles in absence of other, directly adjacent particles, as also reported in the literature [11, 12, 17, 69, 70]. However, when such particles are present, signs of deagglomeration and formation of intergranular voids are increasingly apparent. It should be noted though that such voids are also present to some degree in the pristine electrodes. Intragranular fracture seems to result from compression and subsequent bending of particles and was also observed for $Na_{2/3}Ni_{1/3}Mn_{2/3}O_2$ [9]. For some monolithic particles that appear crack free, a likely explanation is that they are oriented in a way that the cracking planes are parallel to the cross-section plane. A large number of smaller cracks at the particle surface can be observed, with crack tips expanding into the bulk (especially in figures 5(g) and S7(g)), in good agreement with literature reports on P2 SIB CAMs [13, 71], where the crack nucleation and growth from the surface is explained by the P2–O2 transition during cycling [9]. For the 3-$NTMO_2$ material after 50 cycles, at high magnification (figure S8), additional surface corrosion is visible, which is probably related to the disproportionation and subsequent dissolution of Mn [30].

When comparing the samples, a difference in the number of intragranular cracks can be observed. After one cycle, for all materials, deagglomeration has set in, and next to these intergranular voids also some intragranular cracks are visible. At higher cycle numbers, 3-$NTMO_2$ shows both substantially more cracked particles and more intragranular cracks per particle, while intergranular fracture dominates the 7-$NTMO_2$ cathode cross sections. These findings qualitatively confirm the hypothesis that AE2 hits, more prevalent in 3-$NTMO_2$, are correlated with intragranular cracking, while AE3 hits, more prevalent in 7-$NTMO_2$, are correlated with intergranular fracture. With both qualitative and quantitative confirmation of the assignment hypothesis, this work presents a non-invasive, non-destructive method of monitoring formation of both intra- and intergranular cracks by the use of AE.

Further attempts to quantify crack formation via the expected increase in surface area (by Kr-BET and two-electrode electrochemical impedance spectroscopy measurements) did unfortunately not lead to concise results. The conductive carbon black used in the electrodes contributes a far greater specific surface area than the CAMs. Besides, the dissolution of Mn from the materials and subsequent deposition under continuous

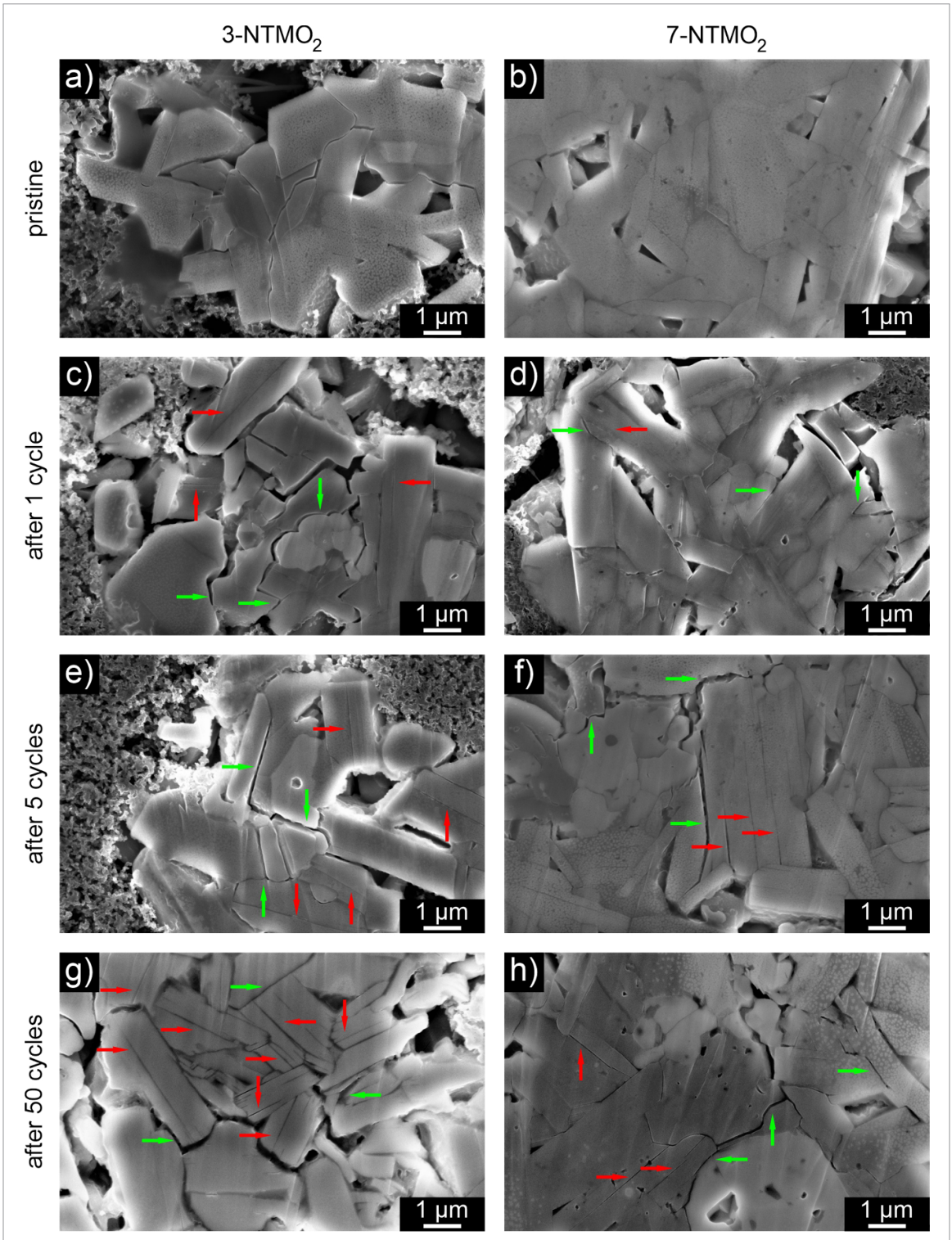

Figure 5. Cross-sectional SEM images of pristine and cycled (fifth and 50th cycle) 3- and 7-$NTMO_2$ cathodes. Arrows exemplify intergranular (green) and intragranular (red) cracks.

SEI formation at the anode [72, 73] leads to a strong rise in impedance, as shown in figure S9, albeit highlighting the effect of increased configurational entropy in suppressing Mn leaching (impedance growth). The role of cathode composition and manufacturing process on AE is outside the scope of this work and will be subject of future investigations.

4. Conclusions

For the first time, AE as a non-destructive characterization technique was applied to SIBs. Three structurally related P2-type CAMs, varying in their configurational entropy and, resulting from that, in the degree of phase transition (two-phase reaction versus solid solution) at potentials above 4.2 V vs. Na^+/Na, were not

only characterized, but also compared to one another. It was found that while acoustic activity in all materials is mainly related to crack formation and propagation, with increasing configurational entropy, it is more concentrated into the initial cycle and at higher peak frequencies. By correlation of electrochemical behavior and AE with *post-mortem* SEM imaging, a lower degree of intragranular fracture and particle delamination was observed with increasing solid-solution-like desodiation. A larger share of acoustic activity, specifically at high peak frequencies, thus stems from particle deagglomeration (intergranular fracture). These results are corroborated quantitatively by *operando* XRD.

It is demonstrated that AE cannot only be used to characterize, but also to compare and evaluate battery materials. Especially, P2-type SIB CAMs show a clear profile with almost only cracking contributing to acoustic activity (and again no effect of gas evolution on the AE). As a non-invasive technique, AE may find further use in battery health monitoring due to the ease of measurement. However, as of now, the complexity of the obtained information requires additional characterization to be interpreted and utilized fully.

Data availability statement

The data that support the findings of this study are available upon reasonable request from the authors.

Acknowledgments

The authors thank Simon Schweidler (Karlsruhe Institute of Technology) for introduction to and assistance with the AE technique and Philipp Quarz (Karlsruhe Institute of Technology) for particle size distribution measurements. Rafael Meinusch and Kilian Vettori (Justus-Liebig-University Giessen) are acknowledged for help with BET measurements and impedance spectroscopy, respectively.

Conflict of interest

The authors declare no conflict of interest.

ORCID iDs

Sören L Dreyer https://orcid.org/0000-0001-8867-4787
Ruizhuo Zhang https://orcid.org/0000-0003-0292-5026
Aleksandr Kondrakov https://orcid.org/0000-0003-1465-2854
Qingsong Wang https://orcid.org/0000-0001-5879-8009
Torsten Brezesinski https://orcid.org/0000-0002-4336-263X
Jürgen Janek https://orcid.org/0000-0002-9221-4756

References

[1] Tarascon J-M 2020 *Joule* **4** 1616–20
[2] Chayambuka K, Mulder G, Danilov D L and Notten P H L 2018 *Adv. Energy Mater.* **8** 1800079
[3] Tapia-Ruiz N *et al* 2021 *J. Phys. Energy* **3** 031503
[4] Chen T, Ouyang B, Fan X, Zhou W, Liu W and Liu K 2022 *Carbon Energy* **4** 170–99
[5] Liu Y, Wang D, Li H, Li P, Sun Y, Liu Y, Liu Y, Zhong B, Wu Z and Guo X 2022 *J. Mater. Chem.* A **10** 3869–88
[6] Lee D H, Xu J and Meng Y S 2013 *Phys. Chem. Chem. Phys.* **15** 3304–12
[7] Sun H-H and Manthiram A 2017 *Chem. Mater.* **29** 8486–93
[8] Yoon C S, Jun D-W, Myung S-T and Sun Y-K 2017 *ACS Energy Lett.* **2** 1150–5
[9] Wang K, Yan P and Sui M 2018 *Nano Energy* **54** 148–55
[10] Kulka A, Marino C, Walczak K, Borca C, Bolli C, Novák P and Villevieille C 2020 *J. Mater. Chem.* A **8** 6022–33
[11] Alvarado J, Ma C, Wang S, Nguyen K, Kodur M and Meng Y S 2017 *ACS Appl. Mater. Interfaces* **9** 26518–30
[12] Liu Y, Fang X, Zhang A, Shen C, Liu Q, Enaya H A and Zhou C 2016 *Nano Energy* **27** 27–34
[13] Wang K, Wan H, Yan P, Chen X, Fu J, Liu Z, Deng H, Gao F and Sui M 2019 *Adv. Mater.* **31** 1904816
[14] Yang Q, Wang P-F, Guo J-Z, Chen Z-M, Pang W-L, Huang K-C, Guo Y-G, Wu X-L and Zhang J-P 2018 *ACS Appl. Mater. Interfaces* **10** 34272–82
[15] Jiang K, Zhang X, Li H, Zhang X, He P, Guo S and Zhou H 2019 *ACS Appl. Mater. Interfaces* **11** 14848–53
[16] Cheng Z *et al* 2022 *Adv. Energy Mater.* **12** 2103461
[17] Fu F *et al* 2022 *Nat. Commun.* **13** 2826
[18] Zhang R-Z and Reece M J 2019 *J. Mater. Chem.* A **7** 22148–62
[19] Miracle D B and Senkov O N 2017 *Acta Mater.* **122** 448–511
[20] Wang Q, Velasco L, Breitung B and Presser V 2021 *Adv. Energy Mater.* **11** 2102355
[21] Sturman J W, Baranova E A and Abu-Lebdeh Y 2022 *Front. Energy Res.* **10** 862551
[22] Amiri A and Shahbazian-Yassar R 2021 *J. Mater. Chem.* A **9** 782–823
[23] Ma Y, Ma Y, Wang Q, Schweidler S, Botros M, Fu T, Hahn H, Brezesinski T and Breitung B 2021 *Energy Environ. Sci.* **14** 2883–905
[24] Chen Y, Fu H, Huang Y, Huang L, Zheng X, Dai Y, Huang Y and Luo W 2021 *ACS Mater. Lett.* **3** 160–70

[25] Ma Y et al 2021 Adv. Mater. 33 2101342
[26] Ma Y et al 2022 Adv. Funct. Mater. 32 2202372
[27] Zhao C, Ding F, Lu Y, Chen L and Hu Y-S 2020 Angew. Chem., Int. Ed. 59 264–9
[28] Yan S, Luo S, Yang L, Feng J, Li P, Wang Q, Zhang Y and Liu X 2022 J. Adv. Ceram. 11 158–71
[29] Lin C-C et al 2022 Energy Storage Mater. 51 159–71
[30] Wang J et al 2022 Mater. Futures 1 035104
[31] Shadike Z, Zhao E, Zhou Y-N, Yu X, Yang Y, Hu E, Bak S, Gu L and Yang X-Q 2018 Adv. Energy Mater. 8 1702588
[32] Zhao E, Zhang Z-G, Li X, He L, Yu X, Li H and Wang F 2020 Chin. Phys. 29 018201
[33] Dreyer S L, Kondrakov A, Janek J and Brezesinski T 2022 J. Mater. Res. 37 3146–68
[34] Bommier C, Chang W, Li J, Biswas S, Davies G, Nanda J and Steingart D 2020 J. Electrochem. Soc. 167 020517
[35] Zhang Y S, Pallipurath Radhakrishnan A N, Robinson J B, Owen R E, Tranter T G, Kendrick E, Shearing P R and Brett D J L 2021 ACS Appl. Mater. Interfaces 13 36605–20
[36] Appleberry M C et al 2022 J. Power Sources 535 231423
[37] Majasan J O, Robinson J B, Owen R E, Maier M, Radhakrishnan A N P, Pham M, Tranter T G, Zhang Y, Shearing P R and Brett D J L 2021 J. Phys. Energy 3 032011
[38] Enoki M, Inaba H, Mizutani Y, Nakano M and Ohtsu M 2016 Practical Acoustic Emission Testing (Tokyo: Springer) (https://doi.org/10.1007/978-4-431-55072-3)
[39] Schweidler S, Bianchini M, Hartmann P, Brezesinski T and Janek J 2020 Batteries Supercaps 3 1021–7
[40] Beganovic N and Söffker D 2019 J. Energy Resour. Technol. 141 041901
[41] Wang K, Chen Q, Yue Y, Tang R, Wang G, Tang L and He Y 2023 Nondestruct. Test. Eval. 38 480–99
[42] Zhang K, Yin J and He Y 2021 Sensors 21 712
[43] Choe C-Y, Jung W-S and Byeon J-W 2015 Mater. Trans. 56 269–73
[44] Kircheva N, Genies S, Chabrol C and Thivel P-X 2013 Electrochim. Acta 88 488–94
[45] Schweidler S, Dreyer S L, Breitung B and Brezesinski T 2022 Coatings 12 402
[46] Kircheva N, Genies S, Brun-Buisson D and Thivel P-X 2011 J. Electrochem. Soc. 159 A18–A25
[47] Tranchot A, Etiemble A, Thivel P-X, Idrissi H and Roué L 2015 J. Power Sources 279 259–66
[48] Tranchot A, Idrissi H, Thivel P-X and Roué L 2016 J. Power Sources 330 253–60
[49] Schiele A, Breitung B, Mazilkin A, Schweidler S, Janek J, Gumbel S, Fleischmann S, Burakowska-Meise E, Sommer H and Brezesinski T 2018 ACS Omega 3 16706–13
[50] Villevieille C, Boinet M and Monconduit L 2010 Electrochem. Commun. 12 1336–9
[51] Schweidler S, Dreyer S L, Breitung B and Brezesinski T 2021 Sci. Rep. 11 23381
[52] Hsu N N 1977 Acoustic emissions simulator US Patent 4,018,084 (available at: https://image-ppubs.uspto.gov/dirsearch-public/print/downloadPdf/4018084)
[53] Etiemble A, Idrissi H and Roué L 2012 J. Acoust. Emiss. 30 54–64 (available at: www.ndt.net/search/docs.php3?id=15395)
[54] Tapia-Ruiz N, Dose W M, Sharma N, Chen H, Heath J, Somerville J W, Maitra U, Islam M S and Bruce P G 2018 Energy Environ. Sci. 11 1470–9
[55] Paulsen J M, Donaberger R A and Dahn J R 2000 Chem. Mater. 12 2257–67
[56] Matsuo T, Uchida M and Cho H 2011 J. Solid Mech. Mater. Eng. 5 678–89
[57] Rhodes K, Dudney N, Lara-Curzio E and Daniel C 2010 J. Electrochem. Soc. 157 A1354–A1360
[58] Didier-Laurent S, Idrissi H and Roué L 2008 J. Power Sources 179 412–6
[59] Ramadan S and Idrissi H 2008 Desalination 219 358–66
[60] Etiemble A, Idrissi H and Roué L 2011 J. Power Sources 196 5168–73
[61] Etiemble A, Idrissi H, Meille S and Roué L 2012 J. Power Sources 205 500–5
[62] Simescu F and Idrissi H 2009 Meas. Sci. Technol. 20 055702
[63] Yan P, Zheng J, Gu M, Xiao J, Zhang J-G and Wang C-M 2017 Nat. Commun. 8 14101
[64] Yan P, Zheng J, Chen T, Luo L, Jiang Y, Wang K, Sui M, Zhang J-G, Zhang S and Wang C 2018 Nat. Commun. 9 2437
[65] Zhang H, Omenya F, Yan P, Luo L, Whittingham M S, Wang C and Zhou G 2017 ACS Energy Lett. 2 2607–15
[66] Somerville J W et al 2019 Energy Environ. Sci. 12 2223–32
[67] Yabuuchi N, Kajiyama M, Iwatate J, Nishikawa H, Hitomi S, Okuyama R, Usui R, Yamada Y and Komaba S 2012 Nat. Mater. 11 512–7
[68] Radin M D, Alvarado J, Meng Y S and Van der Ven A 2017 Nano Lett. 17 7789–95
[69] Hasa I, Passerini S and Hassoun J 2017 J. Mater. Chem. A 5 4467–77
[70] Sengupta A, Kumar A, Barik G, Ahuja A, Ghosh J, Lohani H, Kumari P, Bhandakkar T K and Mitra S 2023 Small 19 2206248
[71] Wang K, Yan P, Wang Z, Fu J, Zhang Z, Ke X and Sui M 2020 J. Mater. Chem. A 8 16690–7
[72] Lee Y K 2021 J. Power Sources 484 229270
[73] Shin H, Park J, Sastry A M and Lu W 2015 J. Power Sources 284 416–27